Defects in Irradiated Silicon: Electron Paramagnetic Resonance and Electron-Nuclear Double Resonance of the Arsenic- and Antimony-Vacancy Pairs

EDWARD L. ELKIN* AND G. D. WATKINS
General Electric Research and Development Center, Schenectady, New York 12301
(Received 19 April 1968)

Two EPR spectra are observed in irradiated silicon (designated Si-*G*23 and Si-*G*24) which are identified with the neutral charge states of a lattice vacancy adjacent to a substitutional arsenic or antimony atom, respectively. EPR and ENDOR studies reveal a high degree of similarity between these defects and the phosphorus-vacancy pair (Si-*G*8) studied previously. Nuclear quadrupole interactions for the As and Sb atoms give additional information about the defect configuration, not available for the phosphorus-vacancy pair. For all three defects, a large static Jahn-Teller distortion occurs. Analysis of the response of the defects to externally applied stress allows an estimate of ≈ 1 eV for the magnitude of the Jahn-Teller stabilization energy. It is concluded that this energy is larger than the electron-electron interaction energies and comparable to (or greater than) the crystal-field energies for the electrons involved in the core of the defects. Studies of the group-V atom-vacancy reorientation kinetics reveal variations between the three defects that can be correlated with the elastic interactions between the oversize arsenic or antimony atoms and the tensile strain around the lattice vacancy. Comparison of the results with the annealing studies of electrical properties by Hirata *et al.* indicate that the annealing of each defect involves the migration of the pair as an entity through the lattice.

I. INTRODUCTION

THE mobility at temperatures well below room temperature exhibited by lattice vacancies in silicon has been established in previous papers in this series.[1–5] Paramagnetic defect centers resulting from the trapping of these vacancies by impurities can assume the configuration of impurity-vacancy pairs, examples of which are the oxygen-vacancy pair[1,2] (*A* center, giving the Si-*B*1 EPR resonance), the aluminum-vacancy pair[6] (giving the Si-*G*9 resonance), and the phosphorus-vacancy pair[3] (*E* center, giving the Si-*G*8 resonance). The divacancy[5] has been observed in *p* type (Si-*G*6 spectrum) as well as in *n*-type (Si-*G*7 spectrum) samples.

The present paper represents a natural extension of the previous work to include defect centers produced by room-temperature electron irradiation of floating-zone silicon samples doped with group-V shallow donor impurities beyond phosphorus, namely, arsenic ($Z=33$) and antimony ($Z=51$). The existence of a net acceptor level at $E_c-(0.43$ eV) in antimony-doped, γ-irradiated silicon has been established by Sonder and Templeton.[7] With less assurance, they also determine a level at $E_c-(0.46$ eV) in similarly treated arsenic-doped samples. These levels, in analogy with an $E_c-(0.47$ eV) level determined for the phosphorus-vacancy pair, were suggested by them to be associated with donor-vacancy complexes in these materials. The assignment as group-V atom-vacancy pairs has also been made for levels at $\approx E_c-(0.4$ eV) found in P-, As-, Sb-, and Bi-doped, γ-irradiated silicon by Hirata *et al.*[8]

In this paper, EPR spectra of electron-irradiated silicon containing either As or Sb are presented and are shown to be amenable to analysis in terms of defect models analogous to the phosphorus-vacancy pair. The evidence leading to this identification will be presented, and various experimental tests of the model will be described.

Although the Sb- and As-vacancy pair spectra do show a high degree of formal similarity to the P-vacancy pair spectrum, they also possess distinctive features not found in the latter. The observation of first-order forbidden $\Delta m \neq 0$ transitions necessitates an extension of the spin Hamiltonian to include second- (and higher-) order effects arising from nuclear quadrupolar interactions. (The *P*-vacancy pair exhibits no quadrupolar interaction since $I=\frac{1}{2}$ for its 100% abundant P^{31} atomic species.) This is seen to be especially true in the case of the As center, in which the presence of normally forbidden transitions of intensities comparable to the allowed transitions introduces a degree of complexity sufficient to preclude our having made a complete analysis of the EPR spectrum.

A more sensitive measurement of the quadrupolar interaction is obtained through ENDOR studies in which such interactions are observed as first-order effects. The ENDOR spectra to be described corroborate the importance of the quadrupolar interactions detected in the EPR spectra, as well as lend support to

* Present address: Department of Biophysics and Medical Physics, University of California, Berkeley, Calif.

[1] G. D. Watkins and J. W. Corbett, Phys. Rev. **121**, 1001 (1961).
[2] J. W. Corbett, G. D. Watkins, R. M. Chrenko, and R. S. McDonald, Phys. Rev. **121**, 1015 (1961).
[3] G. D. Watkins and J. W. Corbett, Phys. Rev. **134**, A1359 (1964), hereafter referred to as I.
[4] G. D. Watkins, in *Proceedings of the Seventh International Conference on the Physics of Semiconductors, Paris 1964, Vol. III*, edited by P. Baruch (Academic Press Inc., New York, 1965), p. 97.
[5] G. D. Watkins and J. W. Corbett, Phys. Rev. **138**, A543 (1965).
[6] G. D. Watkins, Phys. Rev. **155**, 802 (1967).
[7] E. Sonder and L. C. Templeton, J. Appl. Phys. **34**, 3295 (1963).
[8] M. Hirata, M. Hirata, and H. Saito, J. Appl. Phys. (Japan) **5**, 252 (1966).

the model of the defect by providing unambiguous identification of the relevant impurity atoms and information as to the relative sites they occupy in the defect centers.

II. EXPERIMENTAL PROCEDURE

Experimental techniques relevant to these studies have, for the most part, been described in previous publications.[1–5] The silicon samples[9] were floating-zone, n type (either arsenic or antimony $\approx 10^{15}$–10^{16}/cm^3) and were irradiated at room temperature by 1.5-MeV electrons from a resonant transformer accelerator.

EPR studies were done at ≈ 20 kmc/sec and primarily at 20.4°K, most of the measurements being made in dispersion. ENDOR studies were made at 4.2°K using techniques described in I.

III. GENERAL RESULTS AND DISCUSSIONS

A. Summary of Previous Work on Phosphorus-Vacancy Pair

Previous studies (I) have revealed that the phosphorus-vacancy pair is the dominant observable defect produced by 1.5-MeV electron irradiation in phosphorus-doped vacuum floating-zone silicon. Its formation results from the trapping of a mobile lattice vacancy next to a substitutional phosphorus impurity atom, and it is observed in the resonance only in its neutral charge state after the Fermi level has been reduced to $\lesssim E_c - (0.4$ eV) by the room-temperature irradiation. The model of the defect is depicted in Fig. 1 (suitably generalized to allow eventual inclusion of the antimony- and arsenic-vacancy pairs). Of the three silicon atoms surrounding the vacancy, two can be considered as pulling together to form an electron pair bond, while an unpaired electron primarily in the orbital of the remaining silicon atom gives rise to the observed resonance. This distortion can be viewed as a manifestation of the Jahn-Teller effect.

The salient features of the EPR and ENDOR spectra from which the above model was deduced include

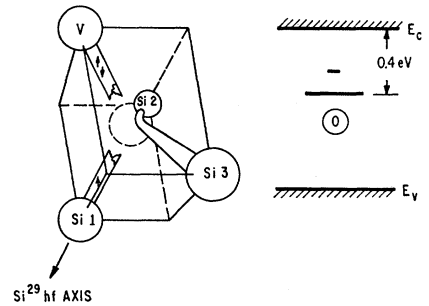

FIG. 1. Model and electrical level position for the group-V atom-vacancy pairs.

[9] Procured from Semiconductor Products Department, General Electric Co., Syracuse, N. Y.

a strong hyperfine interaction with a single silicon atom, as well as a weaker hyperfine interaction with the phosphorus. A linear combination of atomic orbitals (LCAO) construction of the unpaired electron wave function revealed that $\sim 60\%$ of the latter is localized in the dangling orbital on the single silicon atom while $\sim 1\%$ is localized on the phosphorus. The g-tensor has near-axial symmetry with its axis close to the Si^{29} hf axis reflecting the axis of the major portion of the wave function.

In addition to satisfactorily accounting for the above features of the EPR and ENDOR spectra, the model was tested by applying uniaxial stress to the sample at selected temperatures, and also by observing motional broadening and narrowing of the spectrum over a selected temperature range. A detailed account of the spectral alterations expected from these procedures will be deferred until these tests are described for the antimony- and arsenic-vacancy pairs (Sec. IV A); suffice it to say now, however, that the ability to account for the observed changes in the spectrum in terms of the model provided strong additional confirmation of its validity.

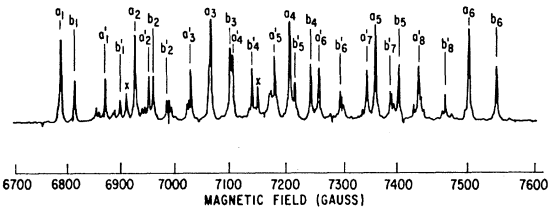

FIG. 2. Antimony-vacancy pair spectrum (SiG-24) at 20.103 kMc/sec with $\mathbf{H}\|\langle 100\rangle$ and $T=20.4$°K.

B. Antimony-Vacancy Pair

1. *Antimony-Vacancy Pair EPR Spectrum (Si-G24)*

A recording of the spectrum (Si-G24) which we identify as arising from the antimony-vacancy pair[10] is shown in Fig. 2 for $\mathbf{H}\|\langle 100\rangle$. The angular dependence of the outermost groups of lines is shown in Fig. 4(a). The complete spectrum can be analyzed as arising from a single anisotropic defect species, but distributed among the various equivalent orientations within the lattice, and described by

$$\mathcal{H}=\beta\mathbf{H}\cdot\mathbf{g}\cdot\mathbf{S}+\sum_j \{\mathbf{I}_j\cdot[\mathbf{A}_j\cdot\mathbf{S}-(\mu_j/I_j)\mathbf{H}] +\mathbf{I}_j\cdot\mathbf{Q}_j'\cdot\mathbf{I}_j\}, \quad (1)$$

with $S=\frac{1}{2}$. Well-resolved hyperfine interactions with the nuclei of two distinct atoms near the defect are observed. One is with a single antimony atom as is evidenced by resolved hyperfine splittings with Sb^{121} (57.25% abundant, $I=\frac{5}{2}$) and Sb^{123} (42.75% abundant,

[10] Like the phosphorus-vacancy pair, this resonance is not observed in the initial stages of irradiation but emerges only at high doses after the antimony shallow donor resonance, originally present, has disappeared. This is consistent with a similar electrical level structure for both centers as shown in Fig. 1.

$I=\frac{7}{2}$) nulcei. In Fig. 2, for instance, the two sets of six lines labeled a_i and b_i ($i=1$ to 6) are each identified with the $(2I+1)$ hyperfine multiplets of Sb^{121} while the other sets of eight (a_i' and b_i') are identified with those of Sb^{123}. The amplitudes and splittings reflect, within the accuracy of measurement, the relative magnetic moments[11] and abundances of the two isotopes.

At higher gain, pairs of satellites symmetrically disposed on either side of each multiplet in the spectrum can also be observed. The intensity per pair is only $\sim 5\%$ of its respective central component and the satellites can therefore only be easily studied at the spectral extremeties, as shown in Fig. 3. These are interpreted as arising from hyperfine interaction with the Si^{29} ($I=\frac{1}{2}$) nucleus of a single neighboring silicon atom, their amplitudes reflecting the isotopic abundance of Si^{29} (4.7%).

From Eq. (1), the energy levels to first order in $Q_j'/|MA_j-(\mu_j/I_j)H|$, and to second order in $A_j/g\beta H$,

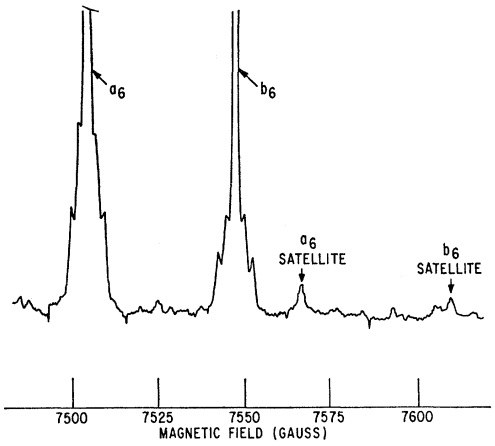

FIG. 3. Part of the Si*G*-24 spectrum, under higher gain conditions than Fig. 2, showing Si^{29} hyperfine satellites.

are given by

$$E=g\beta H+\sum_j E_{hf}{}^j(M,m_j), \tag{2}$$

where

$$E_{hf}{}^j(M,m_j)=\frac{M}{|M|}m_j\{\sum_\alpha [MA_{j\alpha}-(\mu_j/I_j)H]^2 n_{j\alpha}{}^2\}^{1/2}$$
$$+\frac{3m_j{}^2-I_j(I_j+1)}{2}\{\sum_\xi Q_{j\xi}'\eta_{j\xi}{}^2\}+(\langle A_j\rangle^2/2g\beta H)$$
$$\times\{M[I_j(I_j+1)-m_j{}^2]-m_j[S(S+1)-M^2]\}. \tag{3}$$

Here

$$g^2=\sum_i g_i{}^2 n_i{}^2,$$
$$A_j{}^2=\sum_\alpha A_{j\alpha}{}^2 n_{j\alpha}{}^2, \tag{4}$$

[11] Ignoring the small hyperfine anomaly [J. Eisinger and G. Feher, Phys. Rev. **109**, 1172 (1958)], which is of the same order ($\sim 3\%$) as the accuracy of measurement.

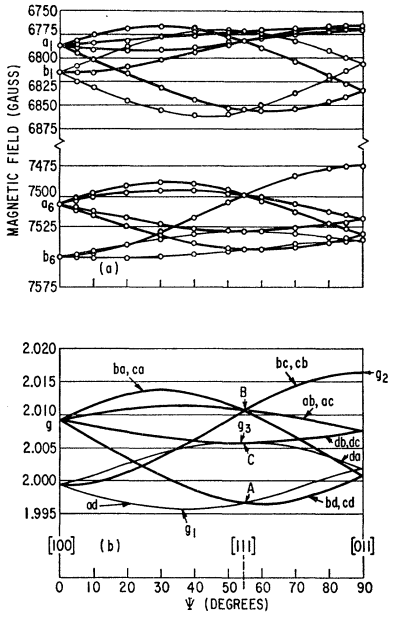

FIG. 4. (a) Angular dependence of the low- and high-field Sb^{121} hyperfine groups of the Si*G*-24 spectrum with **H** in the $(01\bar{1})$ plane (see Fig. 5). The microwave frequency was 20.103 kMc/sec; (b) corresponding g values.

where n_i and $n_{j\alpha}$ are the direction cosines of the magnetic field **H** with respect to the **g** and $\mathbf{A}_j$ tensor principal axes, respectively. The $\eta_{j\xi}$ are the direction cosines of the effective magnetic field seen by the nucleus

$$\mathbf{H}_j=[(MI_j/\mu_j H)\mathbf{A}_j-\mathbf{1}]\cdot\mathbf{H}, \tag{5}$$

with respect to the principal axes of the $\mathbf{Q}_j'$ tensor. In deriving Eq. (3), the small anisotropy in **g** has been ignored as has the anisotropy in $\mathbf{A}_j$ for the second-order hyperfine terms.

With $\mu_j H/I_j \ll A_j$, Eqs. (2) and (3) give for the normally allowed $\Delta M=\pm 1$, $\Delta m_j=0$ EPR transitions, with $S=\frac{1}{2}$,

$$g\beta H\cong h\nu_0-\sum_j\{A_j m_j+(\langle A_j\rangle^2/2g\beta H)$$
$$\times[I_j(I_j+1)-m_j{}^2]\}, \tag{6}$$

which is sufficiently accurate for the EPR analysis.

Using Eq. (6), the g values were determined from the angular dependence of the spectrum and are shown in Fig. 4(b). The principal values and axes of **g**, $\mathbf{A}(Sb^{121})$, and $\mathbf{A}(Si^{29})$ determined from the analysis are given in Table I (with the relevant axes indicated in Fig. 5) for one of the 24 equivalent defect orientations in the lattice.[12]

In Fig. 2, in addition to the multiplets labeled a, b, a', and b', many additional weaker lines can be seen. Most of these can be accounted for as $\Delta m_j \neq 0$ "forbidden"

[12] The values indicated for $A(Sb^{121})$ in the table are actually those determined by ENDOR measurements to be described in Sec. III B2. They are fully consistent with the less accurate [$\pm 1.0(10^{-4})\text{cm}^{-1}$] values determined by the EPR analysis alone.

TABLE I. Spin Hamiltonian parameters for the group-V atom-vacancy pair spectra. (The relevant axes are indicated in Fig. 5.)

Spectrum	Model	$g(\pm 0.0003)$	A (impurity) (10^{-4} cm^{-1})	Q' (impurity) (10^{-4} cm^{-1})	A (Si^{29}) (10^{-4} cm^{-1})
Si-*G*8	$(P^{31}\cdot V)^0$	$g_1=2.0005$	$A_1=(+)\ 10.58\pm0.01$		$A_1=150.0\pm0.5$
		$g_2=2.0112$	$A_2=(+)\ 8.73\pm0.01$		$A_2=\ 98.5\pm0.5$
		$g_3=2.0096$	$A_3=(+)\ 8.64\pm0.01$		$A_3=\ 98.5\pm0.5$
		$\theta=32.3\pm1.0°$	$\theta=\ 163.5\pm0.5°$		$\theta=\ 35.3\pm0.5°$
Si-*G*23	$(As^{75}\cdot V)^0$	$g_1=1.9991$	$(+)\ 16.0\ \pm0.1$		$A_1=149.7\pm1.0$
		$g_2=2.0117$	at	$Q_1'=(-)\ 4.7\pm0.1$	$A_2=\ 98.9\pm1.0$
		$g_3=2.0081$	$\theta=\ 144.7°$		$A_3=\ 98.9\pm1.0$
		$\theta=38.0\pm1.0°$		$\theta=\ 142.7\pm2.0°$	$\theta=\ 35.3\pm0.5°$
Si-*G*24	$(Sb^{121}\cdot V)^0$	$g_1=1.9958$	$A_1=(+)144.49\pm0.05$	$Q_1'=(+)2.927\pm0.002$	$A_1=147.9\pm1.0$
		$g_2=2.0163$	$A_2=(+)131.93\pm0.02$	$Q_2'=(-)1.051\pm0.002$	$A_2=\ 99.2\pm1.0$
		$g_3=2.0058$	$A_3=(+)124.49\pm0.02$	$Q_3'=(-)1.877\pm0.002$	$A_3=\ 99.2\pm1.0$
		$\theta=53.6\pm0.3°$	$\theta=\ 133.2\ \pm0.4°$	$\theta=136.2\pm0.6°$	$\theta=\ 35.3\pm0.5°$

transitions made partially allowed by the quadrupole interaction. In these, the terms in Q_j' and $\mu_j H_j/I_j$ appear in first order and detailed analysis of these transitions would allow the determination of the quantities directly from the EPR studies. However, these are determined more simply and with higher accuracy by ENDOR studies to be described in Sec. III B*2*. We have therefore not attempted to analyze these lines in detail other than to check the position of a few of the prominent ones in order to establish their origin.

It will simplify the presentation to follow if we give labels to the different defect orientations and their corresponding spectra. Following I, we label the four ⟨111⟩ axes of Fig. 5 by the letters *a*, *b*, *c*, and *d*. We can then designate a particular defect orientation by two letters, the first denoting the ⟨111⟩ axis closest to the A_1 axis for the group-V atom (Sb), and the second denoting the ⟨111⟩ direction for the silicon hyperfine axis. In terms of the model (Fig. 1), the first letter corresponds to the ⟨111⟩ axis directed from the vacancy to the neighboring group-V impurity and the second letter corresponds to the ⟨111⟩ axis directed from the vacancy to the silicon neighbor that possesses the unpaired electron. The particular set of principal axes in Fig. 5 can be seen to correspond to those appropriate for the model of Fig. 1, and the defect orientation for both is *cb*. These labels have been used to denote the corresponding *g* values in Fig. 4(b).

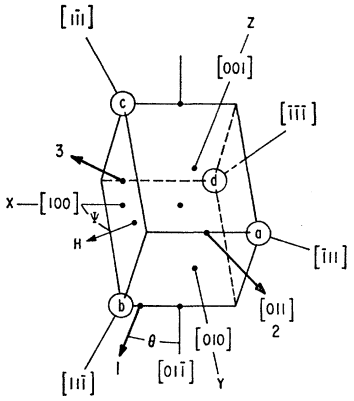

FIG. 5. Principal axes for one of the 24 defect orientations in the lattice of the spectra listed in Table I. The defect model in Fig. 1 is viewed from the same aspect. With the magnetic field **H** in the $(01\bar{1})$ plane as shown, this set of axes gives rise to the *g* values labeled *cb* in Fig. 4.

2. *Antimony-Vacancy Pair ENDOR Spectra*

ENDOR studies were made only on the strong Sb^{121} hyperfine multiplets (not the Si^{29} satellites) and therefore only the hyperfine terms of Eq. (1) for one nuclear species are required. To first order in $Q'/|MA-(\mu/I)H|$ and $A/g\beta H$, the $\Delta m=\pm1$ ENDOR transitions are, from Eq. (3),

$$h\nu(m\rightarrow m-1)\cong\frac{M}{|M|}\{\sum_\alpha[MA_\alpha-(\mu/I)H]^2n_\alpha^2\}^{1/2}+\tfrac{3}{2}(2m-1)(\sum_\xi Q_\xi'\eta_\xi^2). \quad (7)$$

In ignoring higher-order terms, Eq. (7) does not allow a very accurate determination of the principal values of **A** and **Q'**. It does, however, describe the general angular dependence of the spectrum and serves to locate the principal axes of **A** and **Q'** (from the extrema of the sums and differences of the $M=+\frac{1}{2}$ and $M=-\frac{1}{2}$ transitions, respectively).

ENDOR spectra for the *ad* and *da* lines associated with the highest and lowest Sb^{121} multiplets are shown in Fig. 6. Analysis of this data plus similar measurements on the *bc*, *cb* lines gives the principal axes[13] indicated in Table I and Fig. 5.

A general solution for ENDOR transitions to higher order (arbitrary magnetic field orientation) would be very complex because of the anisotropy of **A** and **Q'** and their different principal axes. However, we note that

[13] The extreme quadrupole splittings occur when an axis of **Q'** is parallel to the effective magnetic field seen by the nucleus, given by Eq. (5). With the known anisotropy in **A**, the externally measured difference of 3.5° between Q_1' and A_1 is seen to represent a true deviation of 3.0° at the defect site.

for this defect the **A** and **Q′** axes are within three degrees of each other. *In the particular case of the magnetic field* **H** *oriented along a principal axis* (α) *common to both* **A** *and* **Q′**, the solution is straightforward and gives, for the energy levels to third order in $A/g\beta H$, $Q'/|MA-(\mu/I)H|$,[14]

$$E(M,m)=g_\alpha\beta HM+A_\alpha Mm+\tfrac{1}{2}Q_\alpha'[3m^2-I(I+1)]-(\mu/I)Hm$$
$$+[(A_\beta^2+A_\gamma^2)/4g\beta H]M[I(I+1)-m^2]-(A_\beta A_\gamma/2g\beta H)m[S(S+1)-M^2]$$
$$+[(A_\beta^2+A_\gamma^2)A_\alpha/4(g\beta H)^2]mM[M^2+m^2+1-S(S+1)-I(I+1)]+[A_\alpha A_\beta A_\gamma/2(g\beta H)^2]$$
$$\times[2m^2S(S+1)+2M^2I(I+1)-3M^2m^2-I(I+1)S(S+1)]+\{(Q_\beta'-Q_\gamma')^2/8[MA_\alpha-(\mu/I)H]\}$$
$$\times[2I(I+1)-2m^2-1]m+\tfrac{3}{16}Q_\alpha'\{(Q_\beta'-Q_\gamma')/[MA_\alpha-(\mu/I)H]\}^2$$
$$\times\{5m^4+m^2[7-6I(I+1)]-2I(I+1)+[I(I+1)]^2\}. \quad (8)$$

The allowed $\Delta M=0$, $\Delta m=\pm1$ ENDOR transitions are therefore given by

$$h\nu(M,m',m\rightleftharpoons m-1)=|A_\alpha M-(\mu/I)H+\{\tfrac{3}{2}Q_\alpha'-[(A_\beta^2+A_\gamma^2)/4h\nu_0]M\}(2m-1)$$
$$-(A_\beta A_\gamma/2h\nu_0)[S(S+1)-M^2]+\{(Q_\beta'-Q_\gamma')^2/8[MA_\alpha-(\mu/I)H]\}[2I(I+1)-3-6m(m-1)]$$
$$+[(A_\beta^2+A_\gamma^2)A_\alpha/4h^2\nu_0^2]M[M^2-I(I+1)-S(S+1)+3m^2-3m+2-(2m-1)m']+(A_\alpha A_\beta A_\gamma/2h^2\nu_0^2)$$
$$\times\{[2S(S+1)-3M^2](2m-1)-[S(S+1)-M^2]m'\}+\tfrac{3}{8}Q_\alpha'\{(Q_\beta'-Q_\gamma')/[MA_\alpha-(\mu/I)H]\}^2$$
$$\times\{10m^3-15m^2+m[17-6I(I+1)]+3I(I+1)-6\}|, \quad (9)$$

where m' defines the hyperfine multiplet (m or $m-1$) being observed in the EPR.

Equations (8) and (9) are directly applicable when the magnetic field is along A_2 and Q_2'. We have also used them for the analysis along the other principal axes of **Q′**, the small departure from the corresponding **A** axes, combined with the small anisotropy in **A**, assuring small error. The results are given in Table I. In the analysis, the relative signs of Q_α' and A_α can be determined using the known positive sign of μ. The signs indicated in the table are for an assumed positive value of the A_α. In the analysis, μ/I can be determined directly. The results along the principal axes directions for Q' are

$$|\mu_1|=(3.334\pm0.015)\mu_N,$$
$$|\mu_2|=(3.385\pm0.015)\mu_N,$$
$$|\mu_3|=(3.354\pm0.015)\mu_N.$$

These values compare favorably with the value for Sb^{121} (+3.3415) determined by NMR.[15] The small deviation ($\sim+1\%$) for the value along the 2 axis is probably real. Chemical shifts of this order of magnitude are not unreasonable for such a heavy atom, the anisotropy reflecting the anisotropic nature of its bonds to its neighbors.

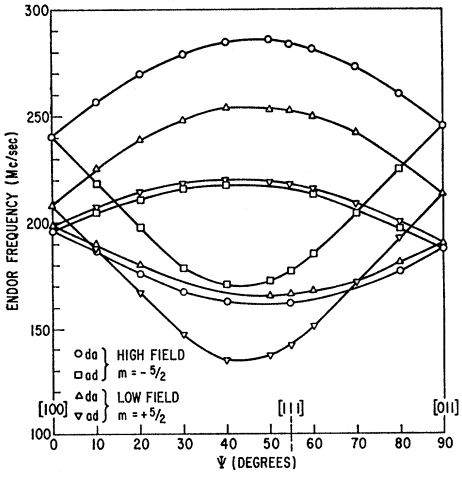

FIG. 6. Angular dependence of the Sb^{121} ENDOR frequencies with **H** in the (01$\bar{1}$) plane. Shown are the transitions for the *ad* and *da* EPR lines associated with the highest and lowest Sb^{121} multiplet groups as shown in Fig. 4.

C. Arsenic-Vacancy Pair

1. Arsenic-Vacancy Pair EPR Spectrum (SiG-23)

Recordings of the arsenic-vacancy pair EPR spectrum[16] are shown in Fig. 7 for **H**$\|\langle100\rangle$ and $\langle111\rangle$. The spectrum is very complex and only well resolved with **H** along the low-index crystallographic directions such as these and the $\langle110\rangle$. As the magnetic field is rotated away from these directions, the lines split and merge together and change intensity, making a detailed angular-dependence study extremely difficult. Since As^{75} is a 100% abundant isotope with $I=\frac{3}{2}$, we might have expected a relatively simple spectrum made up of easily identifiable four-line $\Delta m=0$ hyperfine multiplets throughout. Instead, many additional lines appear to be present. In fact, it is only for **H**$\|\langle111\rangle$ that a set of four equally spaced hyperfine lines is apparent [labelled *C* in Fig. 7(b)]. The additional lines result from the normally forbidden $\Delta m\neq0$ transitions made allowed by

[14] Not included is a term in A^2Q', which is small in our case.

[15] H. Kopeferman, *Nuclear Moments* (Academic Press Inc., New York, 1958), p. 452.

[16] This resonance is also observed only at high doses after the arsenic shallow donor resonance has disappeared, consistent with an electrical level structure as shown in Fig. 1 (see Ref. 10).

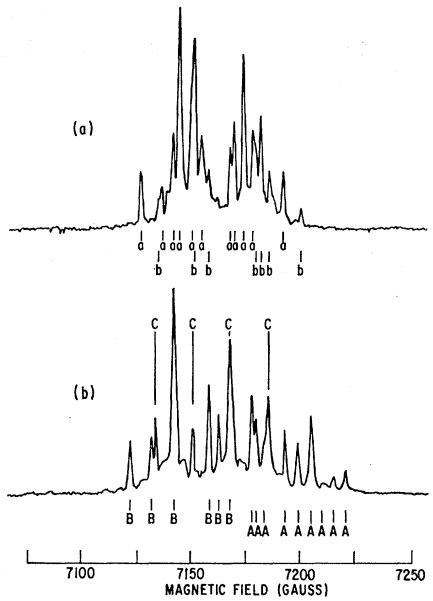

FIG. 7. Arsenic-vacancy spectrum (Si-*G23*) at 20.116 kMc/sec and $T=20.4°$K – (a) $\mathbf{H}\|\langle 100\rangle$; (b) $\mathbf{H}\|\langle 111\rangle$.

a strong nuclear quadrupole interaction which competes with the applied magnetic field as the axis of quantization. The absence of the transitions for one of the defect orientations when $\mathbf{H}\|\langle 111\rangle$ indicates that the principal axis of $\mathbf{Q}'$ lies close to a $\langle 111\rangle$ axis. The intensity of the forbidden lines at other orientations indicates that $|Q'|\sim|A|$. ENDOR studies to be described shortly will make these conclusions more quantitative.

Although it has not been possible to unravel the detailed angular dependence of the spectrum, it has been possible to specify the defect orientations associated with each of the prominent lines for $\mathbf{H}$ along $\langle 100\rangle$, $\langle 111\rangle$, and $\langle 110\rangle$. This identification arises from stress- and temperature-dependent studies to be described in Sec. IV. The number of nonequivalent defect orientations for each magnetic field direction is found in this manner to be identical with that for the antimony-vacancy pair establishing the similar symmetry properties for both centers (e.g., the common g_2, A_2, Q_2' axis is along a $\langle 110\rangle$ axis). For instance, in Fig. 7 we have labelled the lines which are to be identified with the two distinguishable sets for $\mathbf{H}\|\langle 100\rangle$ (a and b) and the three distinguishable sets for $\mathbf{H}\|\langle 111\rangle$ (A, B, and C), in analogy to the corresponding sets for the antimony-vacancy pair.

This identification further allows us to extract the principal values and axes of the g tensor, using the fact that (except for terms of order $A^2/g\beta H$) the center of gravity of the transition is unaltered by the relative magnitudes of $\mathbf{A}$, $\mathbf{Q}'$, and $(\mu/I)H$.[17] In the absence of the $(\mu/I)H$ term, this analysis would be simple because it is easy to demonstrate that the spectrum for each defect orientation would then be symmetrical around its center of gravity. The presence of this term destroys this symmetry, introducing some uncertainty into the determination of the center of gravity. However, with care and with some insight into the identification of the particular transition involved for each multiplet, this uncertainty can be minimized.[18] The g values were estimated in this way for the C lines with $\mathbf{H}\|\langle 111\rangle$, for the a and b lines with $\mathbf{H}\|\langle 100\rangle$, and for the two most distinct sets for $\mathbf{H}\|\langle 110\rangle$ [those corresponding to the ad, da, and the db, dc, ab, ac orientations as shown in Fig. 4(b)].

The four parameters g_1, g_2, g_3, and θ given in Table I were determined from a best fit to these five independent values. The value of A ($\theta=144.7°$) determined from the splitting of the C lines in Fig. 7(b) is 16.1 ± 0.5 (10^{-4}), consistent with the more accurate value given in the table from ENDOR studies. This corresponds in the model to the value of A along the arsenic-vacancy direction.

Si^{29} hyperfine satellites are also observed for this spectrum and again in intensity corresponding to interaction with a single silicon atom site. [Some of the satellites can be seen in Fig. 7(b)]. Again by stress- and temperature-dependent studies they can be correlated with the appropriate defect orientation. Analysis of the splittings with $\mathbf{H}$ along the $\langle 100\rangle$, $\langle 110\rangle$, and $\langle 111\rangle$ directions gives the parameters given in Table I.

2. *Arsenic-Vacancy Pair ENDOR Spectrum*

The ENDOR spectrum, with all of the $|\Delta m|=1, 2, 3$ nuclear transitions for each of the overlapping EPR transitions, is very complex and has not been studied in detail. It has been possible, however, to extract some information about the quadrupole interaction by limited studies on the four C lines of Fig. 7 with $\mathbf{H}$ close to the $\langle 111\rangle$ axis. Angular dependence studies show that the extremum ENDOR frequencies occur when $\mathbf{H}$ is $2.0\pm0.7°$ from the $\langle 111\rangle$ toward the $\langle 100\rangle$ axis. This occurs when the Q_1' axis is parallel to the effective magnetic field direction seen by the nucleus, Eq. (5). The EPR result that the Q_1' axis is close to the $\langle 111\rangle$ is thus confirmed.

In order to locate the Q_1' axis with respect to the crystal axes, it is necessary to take account of the anisotropy of the $\mathbf{A}$ (see Ref. 13). Since the principal axes and values of $\mathbf{A}$ have not been determined, it is not possible to do this accurately. However, making the reasonable assumption that the fractional anisotropy is comparable to that found for the Sb- and P-vacancy pairs, and that the principal axis of $\mathbf{A}$ is close to the $\langle 111\rangle$ as was also

[17] The competition between these terms scrambles the nuclear states for each electronic M state but does not change their mean energy.

[18] For instance, no error is involved for the lines labelled C in Fig. 7(b), because with the principal Q' axis close to the $\langle 111\rangle$ axis and magnetic field direction, the transitions are the normal $\Delta m=0$ allowed transitions. Similarly, because the Q' axis is close to a $\langle 111\rangle$, the first-order quadrupole interaction will be small for $\mathbf{H}\|\langle 100\rangle$, allowing the identification of the outermost a and b multiplets of Fig. 7(a) as the transitions for $\Delta m=0$, again with small error.

found for them, the deviation of the effective field direction seen by the nucleus from that of the external field is estimated to be $<2°$. In Table I, we have therefore taken the Q_1' axis to be that determined directly from the ENDOR angular-dependence studies and have indicated an estimated error large enough to accommodate the possible error arising from the **A** anisotropy.

Most of the $\Delta m=\pm1$, ±2, ±3 nuclear transitions were observed for each of the four C lines. These spectra, analyzed assuming axial symmetry[19] for $\mathbf{Q}'(Q_2'=Q_3'=-\frac{1}{2}Q_1')$ permitted the determination of the parameters Q_1' and $A(\theta=144.7°)$ (the value of A along the arsenic-vacancy direction) given in Table I. Also determined in the analysis was the value for $|\mu|$ of $(1.43\pm0.2)\mu_N$, in good agreement with the value $(+1.4349)$ determined for As^{75} from NMR studies.[20] Using the known sign for μ, the relative signs of A and Q_1' were determined .The values shown in the table are for an assumed positive value for A.

We note that the quadrupolar interaction is indeed of the order of the magnetic hyperfine interaction, $|Q_1'/A|\sim0.3$. This is to be compared with the corresponding ratio for the antimony-vacancy pair of ~0.02.

D. Discussion

1. Relevance of Group-V Atom-Vacancy Pair Model

It is clear from Table I that there is a strong formal similarity between the three spectra: (a) the strong axially symmetric ⟨111⟩ Si^{29} hyperfine interactions reflecting the localization of the electronic wave function primarily in a single dangling bond next to a vacancy; (b) the g tensors also reflecting approximately this axis; (c) the magnetic and electric quadrupole interactions with the group-V atoms reflecting the symmetry of one of the other three atom sites neighboring the vacancy. The principal axes of all of these interactions are consistent with the model of Fig. 1.

In the next sections we will therefore analyze the spin-Hamiltonian parameters for each defect in terms of the model of Fig. 1.

2. Magnetic Hyperfine Interactions

Following the format given in previous publications[1,3,5,6] a linear combination of atomic orbitals centered on atoms near the defect may be used to construct the wave function for the unpaired electron

$$\Psi_{\text{Donor Vac}}=\sum_j \eta_j\psi_j, \tag{10}$$

in which the subscript Donor Vac denotes a phosphorus-, arsenic-, or antimony-vacancy pair.

[19] Equation (3) can be used directly in the case of axial symmetry and with the Q_1' axis parallel to the effective magnetic field direction at the nucleus [Eq. (5)], independent of the relative sizes of Q_1' and A. A slightly better fit to the data can be made with $|Q_2'-Q_3'|\sim0.1|Q_1'|$, using Eq. (8). The values deduced for Q_1' and A (⟨111⟩), however, are essentially the same as those given in the table (within the stated error) and the equations for this analysis are therefore not included in the text.

[20] H. Kopferman (Ref. 15), p. 451.

At each atom site j, ψ_j is approximated as a hybrid $nsnp$ orbital

$$\psi_j=\alpha_j(\psi_{ns})_j+\beta_j(\psi_{np})_j, \tag{11}$$

where $n=3$ for Si and P, $n=4$ for As, and $n=5$ for Sb. For the four nearest-neighbor sites to the vacancy, the p function is taken as directed along the ⟨111⟩ direction from the site to the vacancy center. In the approximation that the hyperfine interaction at the jth nuclear site is determined solely by ψ_j, the axially symmetric form assumed by the interaction parallel and perpendicular to the p-orbital axis is expressed by

$$(A_{\parallel})_j=a_j+2b_j, \tag{12}$$

$$(A_{\perp})_j=a_j-b_j. \tag{13}$$

The Fermi contact interaction gives rise to the isotropic term

$$a_j=(16\pi/3)(\mu_j/I_j)\beta\alpha_j^2\eta_j^2|\psi_{ns}(0)|_j^2, \tag{14}$$

where μ_j is the magnetic moment, and I_j is the spin of the jth nucleus. The anisotropic term results from the dipole-dipole interaction averaged over the electronic wave function and is given by

$$b_j=\tfrac{4}{5}(\mu_j/I_j)\beta\beta_j^2\eta_j^2\langle r_{np}^{-3}\rangle_j. \tag{15}$$

For arsenic and antimony, values of $\langle r_{np}^{-3}\rangle$ were obtained from the experimental optical fine-structure constants of Barnes and Smith,[21] suitably corrected for relativistic effects.[22] Values for $|\psi_{ns}(0)|_j^2$ were obtained by scaling the above values of $\langle r_{np}^{-3}\rangle_j$ by the ratio $|\psi_{ns}(0)|_j^2/\langle r_{np}^{-3}\rangle_j$ calculated from the tabulated Hartree-Fock-Slater wave functions of Herman and Skillman.[23]

This procedure has been described in detail in I, where the corresponding values of Si^{29} and P^{31} were estimated. The results are[24]

$$\begin{aligned}\text{arsenic:}\quad &|\psi_{4s}(0)|^2=93.9(10^{24}\text{ cm}^{-3}),\\ &\langle r_{4p}^{-3}\rangle=49.4(10^{24}\text{ cm}^{-3});\\ \text{antimony:}\quad &|\psi_{5s}(0)|^2=148.1(10^{24}\text{ cm}^{-3}),\\ &\langle r_{5p}^{-3}\rangle=82.3(10^{24}\text{ cm}^{-3}).\end{aligned}$$

Shown in Table II are the results of analysis for α_j^2, β_j^2, and η_j^2 for each of the atom sites of the antimony and arsenic centers, obtained by using Eqs. (10)–(15) in conjunction with the hyperfine constant values given in Table I. The results for the phosphorus-vacancy cen-

[21] R. G. Barnes and W. V. Smith, Phys. Rev. **93**, 95 (1954).

[22] H. Kopferman (Ref. 15), pp. 128 and 446.

[23] F. Herman and S. Skillman, *Atomic Structure Calculations* (Prentice-Hall, Inc., Englewood Cliffs, N. J., 1963), Chap. 6.

[24] The wave functions of Herman and Skillman are presumably less accurate than those of R. E. Watson and A. J. Freeman, Phys. Rev. **123**, 521 (1961), from which our previous estimates for the $3p$ atoms were obtained. As a check, the P values were also estimated from the Herman and Skillman wave functions. Although the values of $|\psi_{3s}(0)|^2$ and $\langle r_{3p}^{-3}\rangle$ were 30% higher than those from the Watson and Freeman wave functions, their ratio was approximately the same, giving a final estimate for $|\psi_{3s}(0)|^2$ within 5% for the two sets of wave functions.

TABLE II. Hyperfine parameters (a_j and b_j) and the corresponding molecular wave-function coefficients (α_j^2, β_j^2, and η_j^2) calculated from the observed hyperfine interaction constants of the group-V atom-vacancy pair spectra.

Defect center	Atom site	a_j (10^{-4} cm^{-1})	b_j (10^{-4} cm^{-1})	α_j^2	β_j^2	η_j^2
P vacancy	Si 1	(−)115.7	(−)17.2	0.14	0.86	0.59
	Si 2	(−) 12.4	···	(0.30)	(0.70)	0.03
	Si 3	(−) 12.4	···	(0.30)	(0.70)	0.03
	P	(+) 9.32	(+) 0.63	0.29	0.71	0.01
As vacancy	Si 1	(−)115.8	(−)16.9	0.14	0.86	0.59
	Si 2	···	···	···	···	···
	Si 3	···	···	···	···	···
	As	(+)(14.4)	(+)(0.8)	(0.32)	(0.68)	(0.01)
Sb vacancy	Si 1	(−)115.5	(−)16.2	0.15	0.85	0.57
	Si 2	(−) 4.6	···	(0.30)	(0.70)	0.01
	Si 3	(−) 4.6	···	(0.30)	(0.70)	0.01
	Sb	(+)400.6	(+)16.3	0.39	0.61	0.04

ter (I) are also included for comparison. The signs indicated for a_j and b_j reflect that of μ_j, as expected from Eqs. (14) and (15). They are enclosed within parentheses to indicate that no experimental verification was possible, since only $|A_{\parallel}|$ and $|A_{\perp}|$ could be determined. In the analysis, the departures from axial symmetry of the group-V hyperfine interactions were ignored. An average value of $(A_{\mathrm{Sb}})_2$ and $(A_{\mathrm{Sb}})_3$ was used for $(A_{\perp})_{\mathrm{Sb}}$. In order to make a rough estimate for the arsenic-vacancy pair for comparison, $A_{\langle 111\rangle}$ was taken as $A_{\parallel}$ and $(A_{\perp})_{\mathrm{As}}$ was estimated by assuming that the ratio $(A_{\perp})/(A_{\parallel})$ for arsenic is intermediate between that of phosphorus and antimony. The average of these two ratios was taken as its value.

Estimates of a_j for the Si 2 and Si 3 sites of the Sb center were obtained from an experiment to be described in a later section. Values of $\alpha^2 \approx 0.30$, $\beta^2 \approx 0.70$ were assumed in order to calculate η^2 for these sites, b_j not being experimentally determined. These values for α_j^2 and β_j^2 were chosen so as to coincide with those determined for a similar configuration in the Si-A center.[1] Estimates of neither a_j nor b_j were available for the arsenic center Si 2 and Si 3 sites.

It is seen from Table II that, for each of the centers, the relative percentage and hybrid character of the wave function located on the respective Si 1 site remain practically unaltered. In each case, ~60% of the total wave function is localized on a single unpaired silicon atom, this portion of the wave function being of ~85% p and ~15% s character. As argued in I, the enhanced p character over that of an sp^3 bond can be construed to indicate a relaxation of the unpaired silicon atom toward its three nearest neighbors and away from the vacancy.

The percentage of $\Psi_{\mathrm{Donor\ Vac}}$ on the impurity atom site is seen to increase with the atomic weight of the atom occupying that site. It is possible to account for only ~1% of the wave function on the phosphorus site, while ~4% is found on the antimony atom in its vacancy-pair center. The composition of the wave function at this site as one goes from phosphorus to antimony is seen to increase from ~30% to ~40% s, and decrease from ~70% to 60% p.

Accompanying the increase in the percentage of $\Psi_{\mathrm{Donor\ Vac}}$, which can be accounted for on the impurity atom site, is a corresponding decrease in the relative percentage on the sites of the two paired silicon atoms. An additional ~6% of $\Psi_{\mathrm{P-Vac}}$ is found on the phosphorus Si 2 and Si 3 sites, whereas only ~2% of $\Psi_{\mathrm{Sb-Vac}}$ can be so accounted for.

For each of the centers, ~70% of its wave function can be accounted for on the localized molecule composed of the four atoms surrounding the vacancy. The remaining ~30% of $\Psi_{\mathrm{Donor\ Vac}}$ is presumably distributed over more distant silicon atoms, and gives rise to the observed structure on the shoulders of lines in the EPR spectra.

3. *Quadrupolar Interactions*

Information regarding the total electronic charge density distribution surrounding the impurity atom nucleus can be obtained from the magnitude and sign of the quadrupolar interaction. The quadrupole constant Q_i' along a principal axis is given by[25]

$$Q_i' = e^2 q_i Q / 2I(2I-1), \tag{16}$$

where eQ is the nuclear electric quadrupole moment and eq_i is the electric field gradient along this axis. Since the magnitude of eq at the nucleus receives its greatest contribution from the lowest partially filled p-type orbitals,[26] the magnitude of Q_i' may be related to the degree of unbalanced charge density in the $4p$ and $5p$ orbitals of As and Sb, respectively. For a single electron in a np orbital, the field gradient is axially symmetric along the axis of the p function, with

$$q_{np} = -\tfrac{4}{5}\langle r_{np}^{-3}\rangle. \tag{17}$$

With our previous estimates of $\langle r_{np}^{-3}\rangle$, and the values[27,28]

$$+0.3(10^{-24}\ \mathrm{cm}^2) \quad \text{and} \quad -0.53(10^{-24}\ \mathrm{cm}^2)$$

for the quadrupole moments of As^{75} and Sb^{121}, respectively, we estimate

$$\begin{aligned} Q_1'(\mathrm{As}^{75})_{4p} &= -23(10^{-4}\ \mathrm{cm}^{-1}), \\ Q_1'(\mathrm{Sb}^{121})_{5p} &= +20(10^{-4}\ \mathrm{cm}^{-1}). \end{aligned} \tag{18}$$

Comparison with the observed values along the impurity-vacancy axis (Table I) indicates an unbalanced charge density in this direction equivalent to ~21% pure $4p$ for the arsenic center and ~15% pure $5p$ for the antimony center. (In this analysis, we ignore the small departure from axial symmetry for $\mathbf{Q}'$.) The signs

[25] T. P. Das and E. L. Hahn, *Nuclear Quadrupole Resonance Spectroscopy* (Academic Press Inc., New York, 1958), p. 17.
[26] C. H. Townes and B. P. Dailey, J. Chem. Phys. **17**, 782 (1949).
[27] H. Schuler and M. Marketu, Z. Physik **102**, 703 (1936).
[28] K. Murakawa, Phys. Rev. **100**, 1369 (1955).

of the $\mathbf{Q}'$, arrived at by assuming A_j positive, indicate an excess of electronic charge density along the impurity-vacancy axis for both centers.

We can refer to the model of Fig. 1 to see if these values are reasonable. As a first estimate, let us assume that the electron density in each of the other three bonding orbitals emanating from the group-V atom (bonding to its neighbors, not shown) corresponds to that of a single electron in the corresponding directed atomic orbital on the atom. Therefore, one of the electrons in the dangling orbital pointing into the vacancy just cancels the field gradient due to the bonding ones, and the remaining field gradient arises from the second electron in the dangling orbital. Using as a guide to the percentage p character in the dangling orbital that deduced from the hyperfine interaction in Table II, we conclude that the field gradient should be that corresponding to an excess electron with 60–70% p character. The observed sign is therefore as expected, and the size, though somewhat lower than this simple model predicts, is of the right order of magnitude.

There are several refinements to the model which would tend to reduce the magnitude of the predicted field gradient: (a) The extra nuclear charge of the group-V atoms should introduce partial ionic character into the bonds with its neighbors, increasing the electronic density in the corresponding directed orbitals on the atom above that estimated above. This serves to cancel part of the field gradient of the extra electron in the dangling orbital; (b) refinements in the one-electron wave functions to include overlap and admixtures between the orbitals on the neighboring atoms as well as configurational interactions should also tend to spread the excess electron density out, decreasing the field gradient.

We therefore conclude that the observed quadrupole interactions are consistent with the model, representing an excess electron density along the impurity-vacancy axis and of a magnitude corresponding to a substantial fraction of unbalanced p character, as predicted.

4. g Tensor

In the case of the phosphorus-vacancy pair, the g tensor is approximately axially symmetric with its principal axis very close to the ⟨111⟩ direction associated with the dangling orbital on the Si 1 atom of Fig. 1. In I we argued that this could be explained satisfactorily through spin-orbit interaction primarily on the Si 1 atom core. As we go, however, from P to As to Sb, the increased concentration of the wave function on the group-V atom (Table II) plus the increased spin-orbit interaction with atomic weight will make the spin-orbit interaction at the group-V atom core also become important. This is apparent in Table I, where the axial symmetry deteriorates and the g_1 axis departs from the Si-vacancy axis progressively as we go to the As- and Sb-vacancy pairs. For antimony, for instance, the atomic spin-orbit interaction is a factor of 20 larger than that for silicon. Therefore, even though only 4% of the wave function is concentrated on the antimony, we might expect comparable contributions from it and the silicon atom. From Table I, we note that the maximum anisotropy (g_2-g_1) for the Sb-vacancy pair is roughly twice that for the P-vacancy pair, consistent with this expectation.

In addition, certain qualitative features of the g-tensor anisotropy can be understood if we consider the contributions to the g shift from the two atoms as simply adding independently. For instance, in I we concluded that for a single dangling atomic orbital, $\Delta g_{\parallel}\sim 0$ and $\Delta g_{\perp}$ is positive and proportional to $\lambda\beta^2\eta^2$. Since the 2 axis is perpendicular to both the Sb- and Si-vacancy axes, we would therefore expect the maximum positive g shift to be along this direction, as observed. On the other hand, it is not possible to reproduce the observed anisotropy in the g_1g_3 plane very well by this approach. It is clear that detailed agreement requires a more sophisticated treatment where contributions of other atom cores are included as well as the effects of interatomic currents, etc.

IV. MOTIONAL EFFECTS

The validity of the defect model presented for the As and Sb centers may be tested in various ways. Spectral alterations produced by the application of uniaxial stress and/or temperature variations may be critically compared with the predictions of the model.

For instance, for the particular group-V atom-vacancy direction shown in Fig. 1, there are two other entirely equivalent configurations, corresponding to bonding Si 1 and Si 3 together and leaving the unpaired electron on Si 2, or Si 1 and Si 2 together, with the unpaired electron on Si 3. These together with the configuration depicted in Fig. 1 represent the three equivalent Jahn-Teller distortions associated with each defect. The energetics and kinetics of thermally activated reorientations among these three equivalent distortions is considered in Sec. IV A, while preferential alignment of the distortion direction caused by uniaxially applied stress will be described in Sec. IV B.

In addition to this electronic reorientation, the impurity atom-vacancy axis may also be preferentially aligned by the application of stress at elevated temperatures. The results of these studies will be described in Sec. IV C.

A. Low-Temperature Linewidth Studies

As the temperature is raised above ~60°K for the As center and ~75°K for the Sb center, both spectra are observed to change similarly, as shown in Fig. 8 for the Sb center. The relatively simplified spectrum at the high-temperature end results from the emergence of lines (such as A_6B_6) at positions intermediate between other lines (such as A_6 and B_6) which had initially

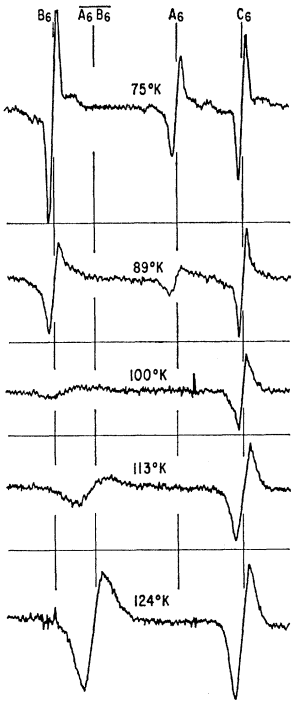

FIG. 8. Antimony-vacancy spectrum (high-field Sb^{121} hyperfine group) versus temperature showing the effect of thermally activated reorientation from one Jahn-Teller distortion direction to another, $\mathbf{H}\|\langle 111\rangle$.

broadened and then eventually disappeared. A brief account of this behavior, suggestive of thermally activated electronic reorientation among the three equivalent Jahn-Teller distortion directions, will be given below. A more complete description is given in I.

Because of the anisotropy of the $\mathbf{g}$ tensor, a multiplet brought into resonance at a particular field value when the defect is in one of its distorted positions will, in general, be thrown out of resonance when the defect reorients to another distortion direction and gives rise to another multiplet at a different field value. If the jumping rate is rapid enough (i.e., the correlation time $\tau \lesssim 10^{-7}$ sec), a lifetime broadening of the spectral lines will result. At higher temperatures the jumping rate becomes so rapid as to average out the g anisotropy, causing motional narrowing and the eventual emergence of a line whose g value represents a weighted average of those of the original multiplets.

For the Sb-vacancy pair, reference to Fig. 4(b) for $\mathbf{H}\|\langle 111\rangle$ indicates three distinguishable g values labeled A, B, and C. These give rise together with the Sb^{121} hf interaction to six sets of lines A_i, B_i, C_i $(i=1, \cdots, 6)$, one such set being shown in Fig. 8(a). For the defect configuration labeling scheme previously described (Sec. III B *1*), the first letter indicates the site of the impurity atom, while the second letter gives the site of the single silicon atom containing the unpaired electron. Thus, the three permissible defect configurations resulting from electronic reorientation around a fixed impurity-vacancy axis direction are obtained by permuting the second letter through the three values not represented by the unchanging first letter. The C_i lines are seen to arise from the defect configurations *da*, *db*, *dc*, which are equivalent when the magnetic field is along the impurity atom-vacancy direction. Since no change in the g value results from electronic reorientation among these three configurations, line C_6 would not be expected to exhibit motional broadening or narrowing. Figure 8 shows that, indeed, this line stays sharp throughout the temperature region. Lines A_6 and B_6 broaden as expected, with A_6 (arising from half as many defect configurations as B_6) approximately twice the width of B throughout the broadening phase. The line A_6B_6 is seen to arise at higher temperatures at a weighted position between A_6 and B_6.

Proceeding as in I, it is possible to deduce the lifetime τ of the reorientation process in both the broadening and narrowing phases. (Because of a poor signal-to-noise ratio and the presence of competing spectra, it was not possible to follow the arsenic center in the motionally averaged phase. For it, only the broadening phase was studied.) These values, plotted versus temperature in Fig. 9, permit an estimate of the activation energy for the process. This will be deferred, however, since results to be described in Sec. IV B allow a more accurate determination to be made. It is noted that the values found here ($E_{As} \approx 0.06$ eV for the As center, $E_{Sb} \approx 0.07$ eV for the Sb center) are very close to that found for the phosphorus-vacancy center (≈ 0.06 eV), and are deemed reasonable values for the type of bond-switching motion postulated.

For the antimony center, the signal-to-noise ratio in the motionally averaged state was adequate to detect the Si^{29} hf satellites. For $\mathbf{H}\|\langle 100\rangle$, the satellites were found

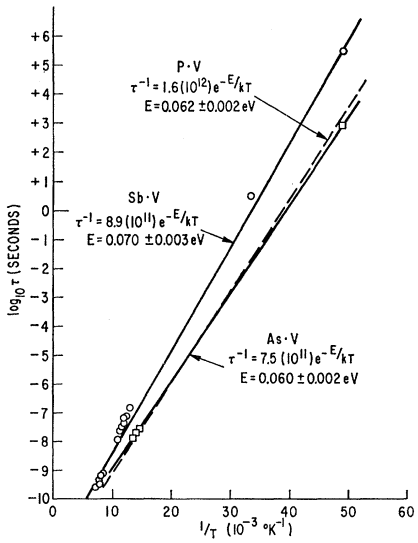

FIG. 9. Lifetime τ of the Jahn-Teller reorientation versus temperature for the three group-V vacancy pair spectra.

to be three times as intense relative to their central component as compared with the low-temperature (20.4°K) spectrum. At the same time, the splitting was reduced to 45.0 G (from 125.3 G). As pointed out in I, this is just what is expected for thermally activated reorientation between the three Jahn-Teller distortions in that the unpaired electron is now effectively smeared over the three silicon sites neighboring the vacancy. Proceeding as in I, the hf interaction $A'(\langle 100\rangle)$ in this state is given by

$$A'(\langle 100\rangle)=\tfrac{1}{3}\sum_i A_i(\langle 100\rangle),$$

in which $A_i(i=1, 2, 3)$ is the strength of the interaction at each of the three silicon sites for the Jahn-Teller distortion direction of Fig. 1. With the measured values of $A'(\langle 100\rangle)$ and $A_1(\langle 100\rangle)$, we can therefore deduce A_2 and A_3, which must be equal by symmetry:

$$|A_2(\langle 100\rangle)|=|A_3(\langle 100\rangle)|=4.6\times 10^{-4}\ \text{cm}^{-1}.$$

These values yield the isotropic constants a_2 and a_3 given in Table II, if the interaction is assumed axially symmetric along a $\langle 111\rangle$ direction.

As mentioned earlier, the arsenic spectrum could not be studied in the motionally averaged state and the corresponding values were therefore not obtained for it.

B. Low-Temperature Stress Studies

It is also possible to study the electronic reorientation described in Sec. IV A by applying a uniaxial stress to the crystal. The application of stress destroys the cubic symmetry of the crystal, under which all possible defect orientations had been equally probable. By adding to a particular Jahn-Teller distortion, for instance, the stress lowers the energy of the defect in that direction and preferential population of this minimal-energy configuration will result.

Figure 10 shows the change in the As-vacancy spectrum under a $\langle 110\rangle$ compressional stress at 20.4°K with the magnetic field along another $\langle 110\rangle$ direction perpendicular to the stress. Similar effects are observed for the Sb-vacancy spectrum, as well as for that of the phosphorus vacancy as reported in I. For these last two, the interpretation is straightforward because their spectra have been completely analyzed and each multiplet can be identified with its specific orientation. For these the dominant effect is a large decrease in the *db*, *dc*, *ab*, *ac* lines with a corresponding increase in the *ad*, *da*. Smaller effects are observed on the other multiplets. We have chosen to show the more complex results for the As-vacancy spectrum, however, to demonstrate the analysis in reverse. Here we have used the analogy with the other centers to help identify the orientations associated with each multiplet. This technique was referred to earlier in Sec. III C.

The recovery of each spectrum from its stress-induced alignment was observed to proceed exponentially with a temperature-dependent time constant τ. For the As

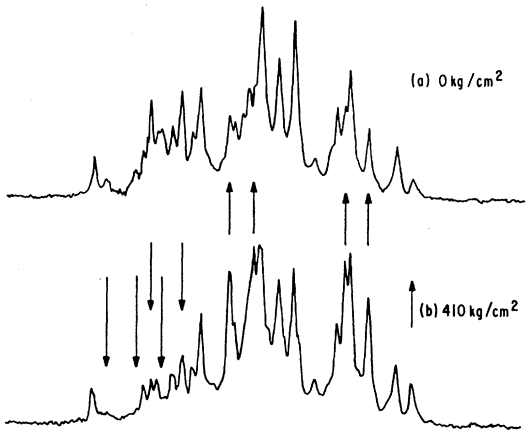

FIG. 10. Change in the arsenic-vacancy pair spectrum (**H**‖[011]) under [01$\bar{1}$] compressional stress at 20.4°K. The lines (indicated by arrows) that decrease in intensity are identified with the *ab*, *ac*, *db*, *dc* defect orientation while those shown as increasing are the *ad*, *da*.

center, $\tau\approx 8.2$ (10^2) sec at 20.4°K, while for the Sb center, $\tau\approx 3.0$ (10^5) sec at 20.4°K and ≈ 3.0 sec at ~ 30°K. Since this time constant τ is the same parameter determined from the linewidth studies of Sec. IV A, these values have been included in Fig. 9 with the linewidth study data for both centers. (The phosphorus-vacancy center result is also shown for comparison. Its experimental points have been omitted, however, to prevent possible confusion with the measured points for these centers.)

The estimates of the activation energies and frequency factors determined from these semilog plots are also indicated in Fig. 9. These values are seen to deviate only slightly for the three centers. The relative independence of the activation energy from the particular impurity atom associated with the defect center may be taken as a further indication that the interpretation primarily in terms of an electronic reorientation among the three silicon neighbors is a valid one.

Now consider the magnitude of the alignment. As has been shown in I, three nonequivalent sets of orientations are created by the $\langle 110\rangle$ stress. If the populations of these sets are assumed to follow a Boltzmann distribution, then the energy differences between the sets may be expressed in terms of two temperatures T_α and T_β given by the relationships

$$\begin{aligned} N_{bc}/N_{bd}&=\exp(-T_\alpha/T),\\ N_{ad}/N_{ab}&=\exp(-T_\beta/T), \end{aligned} \tag{19}$$

with $N_{bc}=N_{cb}$, $N_{ad}=N_{da}$, $N_{bd}=N_{cd}=N_{ba}=N_{ca}$, and $N_{db}=N_{dc}=N_{ab}=N_{ac}$.[29] The observed values of T_α and

[29] We take this opportunity to correct an error in I. There are four nonequivalent sites, as listed above, not three as shown in Fig. 14(a) of I. This error also appears in Ref. 5 as part of Eq. (8). In both cases the error was a typographical one only, the analyses and final results obtained in these papers being correct. We are grateful to Dr. A. Kalma for bringing this error to our attention.

TABLE III. Comparison of the observed and calculated energy differences for the differently oriented defects of the P, As, and Sb centers under the indicated ⟨110⟩ compressional stresses.

Defect center ⟨110⟩ stress	T_j	Observed (°K)	Calculated (°K)	M (eV)
P vacancy 870 kg/cm²	T_α	+ 9	+11	+16.8
	T_β	−90	−94	
As vacancy 410 kg/cm²	T_α	+ 2.5	+ 3.5	+11.0
	T_β	−28.8	−28.8	
Sb vacancy 490 kg/cm²	T_α	− 3.5	+ 4.6	+11.9
	T_β	−37.5	−37.5	

T_β are given in Table III along with those of the phosphorus-vacancy pair center.

For the Sb-vacancy pair, the sample was stressed at 40°K and then cooled with stress on to 20.4°K by filling the crystal with liquid hydrogen. From Fig. 9 we estimate that equilibrium alignment at ~30°K was quenched in by this process. In the analysis of Eq. (19) for this defect, we have therefore used $T=30$°K. For the As-vacancy pair, the reorientation rate was short enough at 20.4°K to allow the application of stress at this temperature.

Proceeding as in I, we take the simple view that only the component of strain along the direction of the two bonding silicon atoms is responsible for the change in energy of a particular defect configuration. We define the change in defect energy per unit strain along this direction as

$$M=(dE/d\epsilon)_{\mathrm{Si-Si}}. \tag{20}$$

Using the measured values of the T_β given in Table III and proceeding with the analysis as in I, the value for the As center is determined to be

$$M_{As}\cong+11.0 \text{ eV/(unit strain)}, \tag{21}$$

while for the Sb center

$$M_{Sb}\cong+11.9 \text{ eV/(unit strain)}. \tag{22}$$

The values of T_α calculated on the basis of these values of M are also given in Table III.

We conclude that the general features of this simple model are confirmed. The observed values of T_α are an order of magnitude smaller than the T_β, as predicted. For the phosphorus and arsenic center, the sign of T_α is also correctly predicted. For the antimony center, it is not. The failure for this center presumably reflects the oversimplified treatment of its coupling to the strain field. In general, this coupling must be expressed by a second-rank tensor, which for a center of this symmetry has three independent components, not just the one given by Eq. (20). Small values for these other components could easily change the sign of T_α without changing the conclusion that the dominant effect is still that of Eq. (20).

In terms of the model, the positive sign for M confirms the expectation that the energy of the defect is lowered when the two bonding silicon atoms are pushed closer together. As argued in I, the size of M is reasonable, being of the order of observed deformation potentials in silicon.

C. High-Temperature Stress Studies

The reorientation of the impurity-atom-vacancy axis from a particular ⟨111⟩ direction to another ⟨111⟩ direction is distinct from the reorientation described in Sec. IV B. Stress alignment of this degree of freedom of the defect occurs at relatively higher temperatures, reflecting the additional energy required to produce this atomic, rather than electronic, reorientation.

Alignment was achieved by applying a ⟨110⟩ compressional stress to the crystals for ~15 min at elevated temperatures in an external squeezing apparatus. After cooling to room temperature with the stress on, the samples were replaced in the cryostat and cooled to 20.4°K in order to monitor the resulting alignment.

Figure 11 shows the changes in the Sb-center spectrum produced by a stress of 3200 kg/cm² applied at a temperature of 110°C. Analysis reveals a degree of alignment in Fig. 11 of

$$\frac{N_\perp}{N_\parallel}=\frac{N_{ad}+N_{ac}+N_{ab}}{N_{bc}+N_{ba}+N_{bd}}\cong1.76. \tag{23}$$

Similar studies of the As-center spectrum resulting from a compressional stress of ≈2500 kg/cm² at 90°C provide an estimate of the observed alignment as ≅1.51.

It is possible to estimate the degree of alignment expected solely in terms of the change in defect energy per unit strain along the Si-Si bond axis direction, using the values of M found in Sec. IV B. Proceeding in a manner similar to the analysis of Sec. IV B, one obtains predicted alignments of 1.36 and 1.23 as compared with the observed values of 1.76 and 1.51, respectively. It is seen that the predicted values are >1, as observed, confirming the expectation of the model that the two bonding silicon atoms prefer to align along the compressed direction. It is possible to bring the predicted values in line with the observed values by extending the above treatment to include another parameter which expresses the change in defect energy per unit strain along the

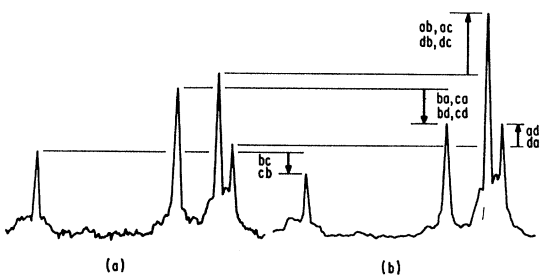

FIG. 11. Antimony-vacancy pair spectrum (high-field Sb^{121} hyperfine group) at 20.4°K, H‖[011]; (a) before and (b) after 3200 kg/cm² [01$\bar{1}$] compressional stress at 110°C.

impurity-atom-vacancy direction. The values for this parameter which represent a best fit to the stress conditions of each center are, for the As center,

$$N_{As}\cong(dE/d\epsilon)_{\text{As Vac}}\cong-6.5\text{ eV/(unit strain)},\quad(24)$$

and for the Sb center,

$$N_{Sb}\cong(dE/d\epsilon)_{Sb\text{ Vac}}\cong-6.1\text{ eV/(unit strain)}.\quad(25)$$

In I a similar value was required for the phosphorus-vacancy center,

$$N_P\cong-9\text{ eV/(unit strain)}.$$

The reorientation kinetics were studied by monitoring the recovery from stress-induced alignment versus annealing. The sample was removed from the cryostat and placed in a bath of boiling water for a 100°C anneal or into a regulated (±0.5°C) oil bath for lower-temperature anneals. The sample was then returned to the cryostat and the remaining alignment monitored at 20.4°K.

The Sb-doped samples were subjected to a series of isothermal anneals at ~100 and ~53°C, similar studies for the As-doped crystals being made at ~73, ~53, and ~35°C. The recoveries exhibited simple exponential behavior, and are compared with the phosphorus-vacancy center result in Fig. 12. The characteristic relaxation times of the reorientation processes were fit to the expected form for a simple thermally activated process.

$$\tau^{-1}=\tau_0^{-1}\exp(-E/kT),\quad(26)$$

with the values of τ_0^{-1} and E for each of the centers given in Table IV.

It is interesting to inquire as to the detailed nature of the reorientation processes associated with the above activation energies. It was shown in I that the reorientation could be interpreted as a four-step process in which the vacancy makes two jumps away from the impurity atom, and then makes two jumps back. The increased value of the activation energy E for reorientation over that for single vacancy motion[30] (~⅓ eV) therefore reflects the fact that some of the binding energy between the vacancy and the impurity must be overcome in removing the vacancy to this next-next-nearest-neighbor position. We expect the binding due to Coulomb interaction to be essentially the same for the three centers so that the differences observed for E presumably arise from elastic interactions. The observed increase in E as we go from phosphorus to arsenic to anitmony correlates with the increasing size of the atom, consistent with the expected interaction of an oversized atom with the tensile strain field around a lattice vacancy. The large variation between the three centers indicates the importance of these elastic effects in the binding.

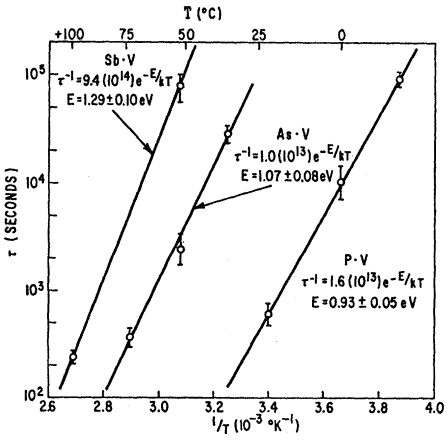

FIG. 12. Characteristic recovery time versus temperature for the group-V atom-vacancy axis reorientation.

TABLE IV. Comparison of kinetics for the group-V atom-vacancy pair reorientation (EPR) with the corresponding $E_c-(0.4$ eV) electric level anneal.[a]

Defect	EPR reorientation τ_0^{-1}(sec^{-1})	EPR reorientation E(eV)	$E_c-(0.4$ eV) level τ_0^{-1}(sec^{-1})	$E_c-(0.4$ eV) level E(eV)
P·V	1.6(10^{13})	0.93±0.05	5(10^7)	0.94
As·V	1.0(10^{13})	1.07±0.08	2(10^8)	1.07
Sb·V	9.4(10^{14})	1.29±0.10	1(10^{10})	1.28

[a] Reference 31.

Reorientation plus impurity-vacancy interchange allows the defect to diffuse as an entity through the lattice. We have no way of directly measuring the kinetics of the impurity-vacancy interchange, but it seems reasonable to assume that its barrier is small compared with the reorientation energy, being more of the order of the value for the isolated vacancy motion (~⅓ eV)[30]. If this is correct, the bottleneck for the diffusion is the reorientation barrier and E in Table IV is also the activation energy for diffusion.

A striking confirmation that this is the case is obtained by comparison with recent annealing studies reported by Hirata *et al.*[31] They studied the annealing kinetics of deep-lying acceptors ($\sim E_c-0.4$ eV) in irradiated floating zone silicon, doped with the different group-V atom donors. In the As- and Sb-doped materials, two annealing stages were observed in the range 100–250°C. The higher-temperature stage was analyzed by these authors to have a characteristic recovery time τ of the form given by Eq. (26) with the values for τ_0^{-1} and E given also in Table IV. Although no estimates of the accuracy have been given by the authors, the agreement with the values determined by the EPR reorientation kinetics is striking. Also shown is their corresponding result for P-doped silicon with its similar agreement, as noted in I. The uniform factor of ~10^5 relating the two values of τ_0^{-1} is consistent with long-range diffusion of the entity for the annealing, with ~10^5 jumps before being trapped by some other defect

[30] G. D. Watkins, J. Phys. Soc. Japan 18, Suppl. II, 22 (1963).
[31] M. Hirata, M. Hirata, H. Saito, and J. H. Crawford, Jr. (to be published); J. Appl. Phys. 38, 2433 (1967).

in the lattice. At the same time, the close agreement serves to confirm that the defect being studied by these authors is correctly identified as that associated with the group-V atom-vacancy pair.

[A lower-temperature annealing stage (~100–150°C) was also observed by Hirata *et al.*[31] which depended upon the doping impurity. For it, the activation energy was higher (1.25 eV for As, 1.74 eV for Sb) with a large preexponential factor more characteristic of a single jump process. The origin of this is not understood and may reflect the property of some other defect interaction with the impurity.]

V. JAHN-TELLER STABILIZATION ENERGY

It is of interest to know the size of the energy associated with the Jahn-Teller distortion. One estimate comes from the character of the unpaired electron wave function itself. This can be seen as follows: In Fig. 13 we sketch a simple one-electron molecular orbital treatment for the electronic structure of the defect. Here the atomic orbitals are the broken bonds (a, b, c, d) of the four atoms surrounding the vacancy. Atom C is the group-V atom, its presence lowering the symmetry from T_d (for the isolated vacancy) to C_{3v}. Because of the extra nuclear charge on the group-V atom, its orbital (a_1) is lowest in energy, the linear combinations of the orbitals on the remaining three silicon atoms splitting into a singlet (a_1) and a doublet (e) as shown. (Small admixtures allowed between the two a_1 states are shown in brackets.)

The neutral state has five electrons, and we populate the molecular orbitals as shown, filling each level before going to the next. (It is not obvious *a priori* that this recipe, which in effect ignores the electron-electron interactions as small compared with the energy between the molecular orbitals, is the correct one. We accept this as an empirical recipe which appears to work[4] for all of the vacancylike defects so far studied in silicon. A theoretical justification for this simple recipe remains to be given.) Because of the partially filled e orbital, the resulting state is degenerate, of E symmetry. It is therefore unstable against a distortion of E symmetry and a Jahn-Teller distortion results as indicated in the figure. If the Jahn-Teller energy were small with respect to the e-a_1 separation before distortion, the distortion shown would cause the wave function for the unpaired electron to be simply

$$6^{-1/2}(2b-a-d)$$

and the percentage of the wave function on the three silicon atoms would be in the ratio 4:1:1. Instead, this ratio is 20:1:1 or greater. This tells us that the Jahn-Teller splitting must be comparable to (or greater than) the e-a_1 spacing resulting in the strong admixture of the wave functions as shown in the figure.

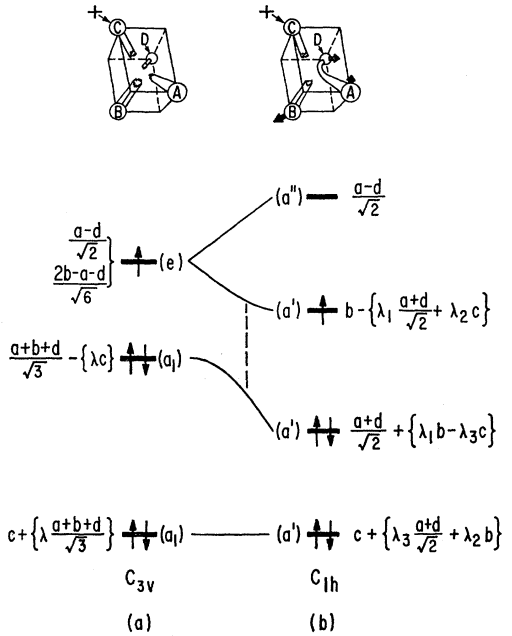

FIG. 13. Simple one-electron LCAO molecular orbital model for the group-V atom-vacancy pair; (a) before and (b) after the Jahn-Teller distortion.

The Jahn-Teller energy is therefore a sizeable energy in the problem, being at least comparable to the "crystal field" energies (as represented by the e-a_1 spacing) and therefore presumably larger in turn than the electron-electron interactions. This is an important observation and means that in a theoretical treatment of a defect like this, the Jahn-Teller effect cannot be "turned on" at the end of the calculation. In the order of a perturbation treatment, it must be included at the outset. As previously pointed out by one of us (G.D.W.),[32] this may have important bearing on previous calculations of vacancies in diamond where the Jahn-Teller effect has been either ignored[33–35] or introduced only at the end of the calculation.[36–38] Indeed, the success of the simple one-electron approach of Fig. 13 for the defects in this paper and for other defects in silicon may well be to a large extent a result of the large Jahn-Teller effect which serves to force a one-electronlike character on the problem.

We can also make a rough estimate of the absolute magnitude of the Jahn-Teller energy. First, let us correct an error in our previous paper (I). There, we at-

[32] A. B. Lidiard, in *Proceedings of the Seventh International Conference on Semiconductors, Paris 1964, Vol. III*, edited by P. Baruch (Academic Press Inc., New York, 1965), p. 335.

[33] C. A. Coulson and M. J. Kearsley, Proc. Roy. Soc. (London) **A241**, 433 (1957).

[34] T. Yamaguchi, J. Phys. Soc. Japan **17**, 1359 (1962); in *Proceedings of the Seventh International Conference on Semiconductors, Paris 1964, Vol. III*, edited by P. Baruch (Academic Press Inc., New York, 1965), p. 323.

[35] A. M. Stoneham, Proc. Phys. Soc. (London) **88**, 135 (1966).

[36] M. Lanoo, thesis, Faculté des Sciences, Orsay, France, 1966 (unpublished).

[37] J. Friedel, M. Lanoo, and G. Leman, *Radiation Effects in Semiconductors*, edited by F. L. Vook (Plenum Press, Inc., New York, 1968), p. 37.

[38] A. B. Lidiard and A. M. Stoneham, in *Science and Technology of Industrial Diamonds*, edited by John Burls (Eyre and Spottiswoode, Ltd., at Grosvenor Press, London, 1967), Vol. I, p. 1.

tempted to relate its magnitude to the energy barrier for thermally activated reorientation from one Jahn-Teller direction to another. This was not correct. As has been shown by Opik and Pryce,[39] the barrier for reorientation for a Jahn-Teller distorted E state bears no simple relation to the Jahn-Teller energy itself, being usually much smaller and arising only from higher-order terms in the Jahn-Teller Hamiltonian.

We can, on the other hand, make an estimate of the Jahn-Teller energy as follows: Consider for simplicity only the "molecule" made up of silicon atoms a, b, and d and their corresponding orbitals. For the wave function that is stabilized by the Jahn-Teller distortion (of e symmetry in C_{3v}, and transforming as a' in the distorted C_{1h} symmetry), the expectation value of the Jahn-Teller Hamiltonian can be written

$$\langle \mathcal{H}(a') \rangle = V_e Q(a') + \tfrac{1}{2} k_e Q(a')^2 , \tag{27}$$

where $Q(a')$ is the component of the e vibrational normal mode of the molecule that also transforms as a' in C_{1h}. Here the quadratic term represents the elastic restoring forces on the atoms while the linear term contains the driving force for the Jahn-Teller effect. Minimizing (27) with respect to $Q(a')$, the energy becomes

$$E = E_{JT} = -V_e^2/2k_e , \tag{28}$$

which is the Jahn-Teller stabilization energy. The resulting equilibrium distortion coordinate is

$$Q_0(a') = -V_e/k_e . \tag{29}$$

Therefore, if we can determine V_e and k_e, we can estimate the Jahn-Teller energy as well as the magnitude of the distortion.

V_e can be estimated experimentally from the stress-alignment experiments described in Sec. IV B. This can be seen as follows: The effect of applied stress on the crystal can be accommodated by rewriting Eq. (27) as

$$\langle \mathcal{H}' \rangle = V_e Q(a') + \tfrac{1}{2} k_e [Q(a') - Q'(a')]^2 , \tag{30}$$

where $Q'(a')$ is the new equilibrium position for this mode under the applied stress (but before the Jahn-Teller distortion). Minimizing this as before with respect to $Q(a')$ gives

$$E' = -V_e^2/2k_e + V_e Q'(a') ,$$

or a change in energy of the defect

$$\Delta E = V_e Q'(a') . \tag{31}$$

In the stress-alignment experiments, we have determined ΔE directly. Assuming that for the atoms surrounding the vacancy the displacement under strain is the same as that of the host atoms, the $Q'(a')$ can be calculated directly from the applied stress and the elastic constants of silicon. The analysis is outlined in the Appendix. The result is that

$$V_e = -\sqrt{2} M/a , \tag{32}$$

where M is the parameter [defined by Eq. (20)] already determined from the stress-alignment studies (Table III), and a is the lattice constant of silicon (5.43 Å). The resulting values of V_e are given in Table V.

TABLE V. Estimates of the Jahn-Teller energy and the magnitude of the distortion for the group-V atom-vacancy pairs.

Defect	V_e (eV/Å²)	E_{JT} (eV)	$Q_0(a')$ (Å)
P·V	−4.38	−1.36	0.61
As·V	−2.87	−0.57	0.40
Sb·V	−3.10	−0.66	0.43

In order to estimate k_e, we take a simple model in which all of the atoms except the three silicon atoms neighboring the vacancy are kept fixed, and only nearest-neighbor central forces are considered. With k the nearest-neighbor force constant, the result is

$$k_e = (22/27)k . \tag{33}$$

With the value for k estimated by Swalin[40] from compressibility data (8.9 eV/Å²), this gives

$$k_e = 7.25 \text{ eV/Å}^2 . \tag{34}$$

The force constant k_e is also given by $\mu\omega_e^2$, where ω_e is the angular frequency of the e vibrational normal mode and μ is the mass of the silicon atom. The value that we have calculated (34) therefore corresponds to a frequency of 6.4 (10^{13}) rad/sec. We note that this is a reasonable value, being comparable to the characteristic frequencies of the perfect lattice. Compare, for instance, to the Raman frequency[41] of 9.85(10^{13}). We have chosen to estimate k_e from our simple model, rather than working back from the phonon curves of the perfect lattice, because the model has built into it the effect of the nearby vacancy.[42]

With (34) and Eqs. (28) and (29), the resulting estimates of the Jahn-Teller energy and the magnitude of the distortion are given in Table V. We see that the energies are indeed large, being of the order of 1 eV. There are, of course, uncertainties in these estimates that are difficult to evaluate. These involve our model for the estimate of k_e as well as the assumption that the atoms neighboring the vacancy move under the applied stress identically to the perfect-lattice atoms. This is the best we can do at this stage, however, and the estimates at least indicate the magnitude of the energies.

Another oversimplification in the model should also be pointed out. We have assumed a linear Jahn-Teller coupling in (27) while a glance at Fig. 13 suggests strong nonlinear effects due to the interaction between the a'

[39] U. Opik and M. H. L. Pryce, Proc. Roy. Soc. (London) **A238**, 425 (1957).

[40] R. A. Swalin, J. Phys. Chem. Solids **18**, 290 (1961).

[41] J. P. Russel, Appl. Phys. Letters **6**, 223 (1965).

[42] We are grateful to A. M. Stoneham, who suggested the model for calculating k_e.

energy levels. In this simple Hartree model, the total electronic energy is just the sum of the one-electron energies. Therefore initially in the distortion the energy is lowered at a rate associated with the single electron in the split-off e state. After the "crossing," the energy lowering approaches twice this rate since two electrons are now in the a' orbital being lowered. In our stress-alignment experiment, the V_e that we measure corresponds to the *slope* of the electronic energy versus $Q(a')$ at the equilibrium distortion position. Therefore Eq. (27) really reflects an equivalent linear Jahn-Teller Hamiltonian that would exist if the e-a_1 splitting were zero and that would give rise to the existing distortion coordinate $Q_0(a')$. It tends to overestimate the Jahn-Teller energy, but again not grossly, the error always being less than the e-a_1 separation.

This nonlinear Jahn-Teller coupling, on the other hand, gives a natural explanation for the strong static character of the distortion. As we have mentioned earlier, a doublet state in the presence of a strictly linear Jahn-Teller coupling and pure harmonic restoring forces has an infinity of distortion positions, with no energy barrier for reorientation.[43] Anharmonic terms in the restoring forces[39] or nonlinear terms in the Jahn-Teller coupling,[44] on the other hand, can serve to stabilize a specific distortion. In particular, it is straightforward to show that, in the presence of coupling between the a' states, the sum of the one-electron energies of Fig. 13 is a minimum for the specific distortion given in the figure.[45] This simple one-electron molecular orbital approach therefore has built into it the necessary nonlinearity to predict the strength and sense of the static distortion as well.

VI. SUMMARY

We conclude that the Si-$G23$ and Si-$G24$ EPR spectra described in this paper arise from the neutral charge state of a lattice vacancy adjacent to a substitutional arsenic or antimony atom, respectively. They are therefore formally equivalent to the Si-$G8$ spectrum which was previously identified as the corresponding phosphorus-vacancy pair. The electrical properties of all three defects are similar, each introducing a single net acceptor level at $\sim E_c-(0.4$ eV). [Small but measurable differences ($\sim 10\%$) in the exact level position for the defects appear to be indicated from the work of Sonder and Templeton.[7]]

For all three, the ground state of the defect is characterized by a Jahn-Teller distortion as shown in Fig. 1 in which two of the three silicon atoms neighboring the vacancy pull together to form an electron-pair bond, with the unpaired electron primarily in a dangling orbital on the remaining silicon atom. Analysis of the hyperfine interactions shows a very close similarity between the centers with $\sim 60\%$ of the wave function on the single silicon atom site for each. Another 6–7% of the wave function is accounted for on the three other atoms neighboring the vacancy, with a tendency as we go from P to As to Sb to increase the concentration on the group-V atom (1–4%) at the expense of the other silicon atoms. The remainder of the wave function is presumably spread out over more distant silicon atoms. The additional information obtained from the quadrupole interaction at the As and Sb sites is consistent with the model.

We conclude that the magnitude of the Jahn-Teller stabilization energy is large, being of the order of 1 eV. It appears to be larger than the electron-electron interaction energies and comparable with (or possibly greater than) the crystal field energies for the valence electrons involved in the core of the defect. It is therefore clearly important in determining the electronic structure of the defect and any theoretical treatment of the defect should include the distortion at the outset in the calculation.

For all three defects, the Jahn-Teller distortion at low temperatures is a static one, with a barrier for reorientation measured to be ~ 0.06 eV. A simple one-electron molecular orbital treatment of the defect has been outlined which gives a natural explanation for the static character of the distortion as well as the character and sense of the distortion involved.

The kinetics of the group-V atom-vacancy reorientation have also been studied and compared with recent annealing studies by Hirata *et al.* The close correlation indicates that annealing of the defect involves migration of the pair as a unit through the lattice.

In our previous paper on the phosphorus-vacancy pair, we used the information gained about the phosphorus-vacancy interaction to estimate the activation energy for silicon self-diffusion (a quantity which had not been measured at the time) and in turn to estimate the formation energy of the lattice vacancy. In particular, we pointed out that for a monovacancy diffusion mechanism, the activation energy for phosphorus diffusion in silicon should be lowered from that of silicon self-diffusion by the binding energy of the vacancy and phosphorus when separated to their next-next-nearest positions. Taking this binding to be 0.28 ± 0.15 eV (deduced from a simple Coulomb binding model), and using the measured value of 3.66 ± 0.18 eV for the phosphorus diffusion,[46] we estimated the silicon self-diffusion energy to be 3.94 ± 0.33 eV. Similarly, with the

[43] J. H. Van Vleck, J. Chem. Phys. **7**, 72 (1939).

[44] A. D. Liehr and C. J. Ballhausen, Ann. Phys. (N. Y.) **3**, 304 (1958).

[45] We compare the energy for this sign of the $Q(a')$ distortion with that of the opposite sign. Since both preserve C_{1h} symmetry (which has a mirror symmetry plane), each must be an extremum, one the minimum and the other the maximum energy configuration. The difference between the two should therefore be the barrier. Since we measure the barrier, it is clear that this simple Hartree model could be pushed further quantitatively. Attempts have been made in this regard, with some success, but they will be deferred to a subsequent publication.

[46] C. S. Fuller and J. A. Ditzenberger, J. Appl. Phys. **27**, 544 (1956).

measured diffusion activation energies[46] for As of 3.52 $\pm$0.17 eV and for Sb of 3.91$\pm$0.19 eV, and the same Coulomb value for the binding energy, we obtain 3.80 $\pm$0.32 and 4.19$\pm$0.34 eV, respectively, also consistent with this estimate.

Recently, however, several authors have measured silicon self-diffusion directly by radioactive tracer methods and obtain 5.13$\pm$0.07,[47] 4.75,[48] and 4.7 eV[49] for the activation energy. Other recent less direct estimates of 4.84$\pm$0.86,[50] 4.2,[51] and 4.5$\pm$0.4 eV[52] also indicate a higher value than our estimate. The reason for this discrepancy is not clear. One possibility is that we have underestimated the binding energy substantially (although a $\sim$1 eV error is difficult to justify). A more likely possibility, we believe, is that either (or both) of the measured high-temperature group-V atom or silicon diffusion is not via the vacancy mechanism at all, making our analysis inappropriate. Evidence for this is particularly strong in the case of self-diffusion, where unusually large pre-exponential factors ($D_0 \sim 10^3$) were found. Ghoshtagore[53] and Peart[48] have interpreted this to indicate that the high-temperature silicon self-diffusion may be via a divacancy mechanism. Seeger and Swanson,[54] on the other hand, argue for an "extended" interstitial mechanism. In any event, there does appear to be a possible inconsistency with the single-vacancy mechanism and further work will be necessary before this question is resolved.

If the group-V atom diffusion is still via a monovacancy mechanism (the pre-exponential factors are somewhat more reasonable, being of the order of $\sim$10), then our previous analysis continues to have significance. The self-diffusion that we estimated would correspond to the monovacancy *contribution* to self-diffusion, and the corresponding estimate of the vacancy formation energy,

$$W = 3.6 \pm 0.5 \text{ eV},$$

would still be valid. However, again, because of the uncertainty involved as to the diffusion mechanisms involved, this estimate must also be considered correspondingly uncertain.

ACKNOWLEDGMENTS

Helpful conversations with F. S. Ham and A. M. Stoneham are gratefully acknowledged. We are also grateful to M. Hirata, M. Hirata, and H. Saito for communicating their results to us prior to publication.

[47] B. J. Masters and J. M. Fairfield, Appl. Phys. Letters **8**, 280 (1966).
[48] R. F. Peart, Phys. Status Solidi **15**, K119 (1966).
[49] R. N. Ghoshtagore, Phys. Rev. Letters **16**, 890 (1966).
[50] W. R. Wilcox and T. J. Chapelle, J. Appl. Phys. **35**, 240 (1964).
[51] H. P. Bonzel, Phys. Status Solidi **20**, 493 (1967).
[52] M. Yoshida and K. Saito, J. Appl. Phys. (Japan) **6**, 573 (1967).
[53] R. N. Ghoshtagore, Phys. Status Solidi **20**, K89 (1967).
[54] A. Seeger and M. L. Swanson, in International Symposium on Lattice Defects in Semiconductors, Tokyo, 1966 (unpublished).

APPENDIX

The defect-labeling scheme of the text serves as a convenient labeling scheme for the $Q_e(a')$ normal modes. Q_{ij} is thus the normal e vibrational mode that stabilizes the ij defect. (Since the first letter denotes the group-V atom, it is the motion of the three remaining atoms in their common plane that is involved. The second letter denotes the atom which moves symmetrically away from the other two. Shown in Figs. 1 and 13 is Q_{cb}.) Referring to the axes of Fig. 5, the relevant normal modes can be expressed in terms of the six strain components ($\epsilon_{xx}, \epsilon_{yy}, \epsilon_{zz}, \epsilon_{yz}, \epsilon_{zx}, \epsilon_{xy}$) by

$$\begin{aligned}
Q_{ca}' &= (-1, 2, -1, -1, 2, -1)a/6\sqrt{2}, \\
Q_{cd}' &= (-1, -1, 2, -1, -1, 2)a/6\sqrt{2}, \\
Q_{cb}' &= (2, -1, -1, 2, -1, -1)a/6\sqrt{2}, \\
Q_{ac}' &= (-1, 2, -1, 1, 2, 1)a/6\sqrt{2}, \\
Q_{ab}' &= (-1, -1, 2, 1, -1, 2)a/6\sqrt{2}, \\
Q_{ad}' &= (2, -1, -1, -2, -1, 1)a/6\sqrt{2}, \text{ etc.},
\end{aligned}$$

where a is the lattice constant of silicon (5.431 Å).

A. ⟨110⟩ Stress

For compressional stress P along the $[01\bar{1}]$ axis (Fig. 5), the strains can be expressed in terms of the elastic moduli, giving

$$\begin{aligned}
Q_{cb}' = Q_{bc}' &= (S_{11} - S_{12} - S_{44})Pa/6\sqrt{2} \\
&= -2Q_{ca}' = -2Q_{ba}' = -2Q_{cd}' = -2Q_{bd}', \\
Q_{ad}' = Q_{da}' &= (S_{11} - S_{12} + S_{44})Pa/6\sqrt{2} \\
&= -2Q_{ab}' = -2Q_{db}' = -2Q_{ac}' = -2Q_{dc}'.
\end{aligned}$$

With

$$N_{ij} \sim \exp(-V_e Q_{ij}'/kT)$$

and

$$\begin{aligned}
N_{bc}/N_{bd} &= \exp(-T_\alpha/T), \\
N_{ad}/N_{ab} &= \exp(-T_\beta/T),
\end{aligned}$$

we obtain

$$\begin{aligned}
kT_\alpha &= V_e(S_{11} - S_{12} - S_{44})Pa/4\sqrt{2}, \\
kT_\beta &= V_e(S_{11} - S_{12} + S_{44})Pa/4\sqrt{2}.
\end{aligned}$$

B. ⟨100⟩ Stress

For compressional stress along the [100] axis of Fig. 5, the corresponding result is

$$\begin{aligned}
Q_{cb}' = Q_{bc}' = Q_{ad}' = Q_{da}' &= -(S_{11} - S_{12})Pa/3\sqrt{2} \\
&= -2Q_{ca}' = -2Q_{cd}' = -2Q_{ba}' = -2Q_{bd}' \\
&= -2Q_{ac}' = -2Q_{ab}' = -2Q_{db}' = -2Q_{dc}'.
\end{aligned}$$

With

$$N_{bc}/N_{bd} = \exp(-T_\gamma/T)$$

as defined in I, we obtain

$$kT_\gamma = -V_e(S_{11} - S_{12})Pa/2\sqrt{2}.$$

For both types of stresses, the formulas are identical with those of I if

$$V_e = -\sqrt{2}M/a.$$